

Quantized circular dichroism on the edge of quantum Hall systems: The many-body Chern number as seen from the edge

F. Nur Ünal^{§,1,*}, A. Nardin^{§,2,†} and N. Goldman^{3,4,‡}

¹*TCM Group, Cavendish Laboratory, University of Cambridge, JJ Thomson Avenue, Cambridge CB3 0HE, United Kingdom*[§]

²*Université Paris-Saclay, CNRS, LPTMS, 91405 Orsay, France*

³*Laboratoire Kastler Brossel, Collège de France, CNRS, ENS-PSL University, Sorbonne Université, 11 Place Marcelin Berthelot, 75005 Paris, France*

⁴*CENOLI, Université Libre de Bruxelles, CP 231, Campus Plaine, B-1050 Brussels, Belgium*

(Dated: July 8, 2024)

Quantum Hall states are characterized by a topological invariant, the many-body Chern number, which determines the quantized value of the Hall conductivity. Interestingly, this topological property can also be accessed through a dissipative response, by subjecting the system to a circular drive and comparing excitation rates obtained for opposite orientations of the drive. This quantized circular dichroism assumes that only the bulk contributes to the response. Indeed, in a confined and isolated system, the edge contribution exactly cancels the bulk response. This work explores an important corollary of the latter observation: If properly isolated, the circular dichroic response stemming from the edge of a quantum Hall droplet must be quantized, thus providing an appealing way to probe the many-body Chern number. Importantly, we demonstrate that this quantized edge response is entirely captured by low-energy chiral edge modes, allowing for a universal description of this effect based on Wen’s edge theory. Its low-energy nature implies that the quantized edge response can be distinguished from the bulk response in the frequency domain. We illustrate our findings using realistic models of integer and fractional Chern insulators, with different edge geometries, and propose detection schemes suitable for ultracold atoms. Edge dichroic responses emerge as a practical probe for strongly-correlated topological phases, accessible in cold-atom experiments.

Introduction— Since the discovery of the quantum Hall (QH) effects [1], the robust quantization of macroscopic observables has been established as the emergence of topology in physics [2–5], sparking tremendous attention in both solid state [6, 7] and quantum engineered settings [8, 9]. This vast exploration of topological states has revealed various quantized effects, accessible through a rich variety of experimental probes, such as transport, interferometry, spectroscopy and tomography [6–9].

Coupling light to topological matter can lead to novel phenomena [10–12], and in particular, to quantized optical responses [13–23]. As a prominent example, circular dichroism (CD) has been proposed as a powerful probe for extracting many-body topological invariants and quantum geometry in a broad class of topological systems [15, 23–35]. This approach has been demonstrated in ultracold atoms, where the CD response was measured to evaluate the Chern number of Floquet-engineered Bloch bands [36]; it was also applied in solid-state qubit systems to extract the full quantum geometric tensor [37–40] and to reveal exotic monopoles [41, 42]. The quantized CD response of strongly-correlated fractional Chern insulators, which reflects the underlying many-body Chern number [34], was also demonstrated through numerical studies [25].

Crucially, the relation between the many-body Chern number of a 2D Chern insulator and its quantized CD response implicitly assumes that the measured response entirely emanates from the bulk [15, 34, 43, 44]. In fact, in a confined and isolated system (e.g. a quantum gas in a trap), the edge contribution to the CD response ex-

actly cancels the (quantized) bulk response [Fig. 1(a)], which can be traced back to the absence of conductivity in closed settings. Identifying schemes that isolate the bulk response [15] has thus been essential in this quantized CD framework.

In this work, we follow a different approach and set the focus on the quantized CD response associated with the edge of quantum Hall systems. We demonstrate that this quantized CD response is entirely captured by low-energy edge modes, as described by Wen’s chiral Luttinger liquid (χ LL) theory [45–48]. This result has multiple consequences: (i) the edge CD response is universal, and can thus be extracted from the edge of any QH state; (ii) the bulk and edge CD responses, which are both quantized in insulating states, can be individually isolated by resolving the dichroic response in the frequency domain [Fig. 1(b)]. We argue that these quantized responses can be individually measured in cold-atom experiments [36], in the presence of well-designed trapping potentials [49, 50]. We illustrate our findings by employing realistic models of Chern insulator (CI) and fractional Chern insulator (FCI) states, considering different edge geometries and edge-mode configurations.

Quantized CD and low-energy edge theory— We consider a general class of Chern insulators characterized by the many-body Chern number, C_{MB} . Such gapped many-body states exhibit a quantized Hall response, $\sigma_{xy}/\sigma_0 = C_{\text{MB}}$, where σ_0 denotes the conductivity quantum [3]. Interestingly, one can relate this transport coefficient to a dissipative optical response, using Kramers-Kronig relations [51]: $\sigma_{xy} = (2/\pi) \int_0^\infty \omega^{-1} \sigma_{xy}^I(\omega) d\omega$. Here, the op-

tical Hall conductivity $\sigma_{xy}^I(\omega)$ can be expressed in terms of excitation rates upon circular driving [15]

$$\sigma_{xy}^I(\omega) = \hbar\omega(\Gamma_+ - \Gamma_-)/8AE^2, \quad (1)$$

where E is the strength of the perturbing electric field $\mathbf{E}_{\pm}(\mathbf{r}, t) = E(\hat{e}_x \pm i\hat{e}_y)e^{-i\omega t} + \text{c.c.}$, $\Gamma_{\pm}(\omega)$ are the excitation rates associated with polarization \pm and frequency ω , and A is the system's area. Combining these results indicates that the many-body Chern number can be directly related to integrated excitation rates [15, 25, 34]

$$\frac{\hbar^2}{2AE^2} (\Gamma_+^{\text{int}} - \Gamma_-^{\text{int}}) = C_{\text{MB}}, \quad (2)$$

where we introduced the notation $\Gamma_{\pm}^{\text{int}} = \int_0^{\infty} \Gamma_{\pm}(\omega)d\omega$. Quantized circular dichroism [Eq. (2)] was measured in quantum engineered systems, where the excitation rates upon circular driving can be finely monitored, e.g. using band-mapping techniques [36]. This quantization law was also verified numerically for FCIs [25].

Crucially, Eq. (2) concerns a pure *bulk* response; it implicitly neglects any contribution from edge modes to the excitation rates. In fact, for any isolated and confined system, the edge and bulk responses perfectly cancel each other [15, 43, 44]

$$(\Gamma_+^{\text{int}} - \Gamma_-^{\text{int}})_{\text{edge}} = -(\Gamma_+^{\text{int}} - \Gamma_-^{\text{int}})_{\text{bulk}}, \quad (3)$$

which can be traced back to the vanishing Hall conductivity of any isolated setting with boundaries. For a non-interacting system, this can be appreciated by noting that the CD response in Eq. (2) can be expressed in terms of the local (real-space) Chern marker [15, 52]

$$\frac{\hbar^2}{2E^2} (\Gamma_+^{\text{int}} - \Gamma_-^{\text{int}}) = \sum_{\mathbf{r}} C_{\mathbf{r}}. \quad (4)$$

As illustrated in Fig. 1(a), the bulk contributes to the quantized response in Eq. (2), $\sum_{\text{bulk}} C_{\mathbf{r}} = AC_{\text{MB}}$, which is exactly compensated by the edge response, $\sum_{\mathbf{r}} C_{\mathbf{r}} = 0$. As a corollary, isolating the edge CD response gives direct access to the many-body Chern number, an intriguing manifestation of the bulk-edge correspondence.

This latter observation brings us to further investigate the CD response associated with edge modes, the nature of which is a priori not obvious. Here, we show that it is entirely associated with the low-energy *gapless* modes localized at the boundary of the system; see Fig. 1(b,c). The quantized edge dichroism can indeed be understood from the viewpoint of the χ LL theory in the large particle-number ($N \gg 1$) limit. For simplicity, we first consider a QH droplet with a circular boundary and a single chiral edge mode, such as an integer QH state [53, 54] or a Laughlin fractional QH state [55] at filling fraction $\nu = -C_{\text{MB}}$ in the lowest Landau level. Generalizations to states with non-circular boundary [56]

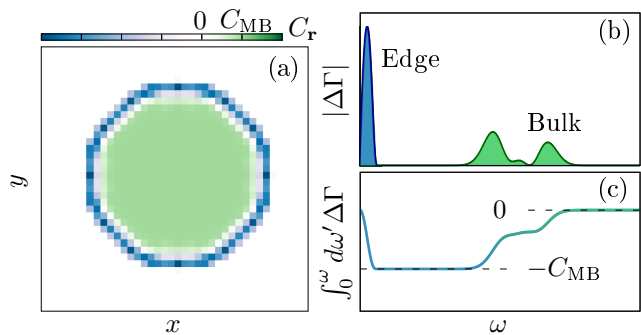


FIG. 1. (a) The dichroic response of a QH state is quantized in the bulk according to the many-body Chern number C_{MB} [Eq. (2)]. In a confined system, this bulk response is perfectly cancelled by the edge, as evidenced by the local Chern-marker description [Eq. (4)]. (b) The bulk and edge dichroic responses can be resolved in the frequency domain. (c) The response associated with low-energy edge modes is quantized, reflecting the many-body Chern number C_{MB} of the topological insulating state.

or with multiple edge modes (e.g. hierarchy [47, 57] or bilayer [58] states, or states with reconstructed edges [59–61]) are presented in Ref. [62].

It is useful to introduce matrix elements

$$S_{\pm} = \sum_{n \in \text{edge}} \left| \int (x \pm iy) \langle n | \hat{\rho}(\mathbf{r}) | 0 \rangle d\mathbf{r} \right|^2 = \sum_{n \in \text{edge}} M_{\pm}^{n,0}, \quad (5)$$

where $\hat{\rho}(\mathbf{r})$ is the particle density operator, $|0\rangle$ denotes the ground state and the sum runs over the set of low-energy collective edge modes [47]. These matrix elements can be related to the integrated rates entering Eq. (3), $(\Gamma_{\pm}^{\text{int}})_{\text{edge}} = 2\pi E^2 S_{\pm} / \hbar^2$, using Fermi's golden rule [15, 44, 62, 63]. Since the bulk is incompressible, contributions to S_{\pm} can only come from a thin layer at the edge of the system, at radius R , with a typical thickness set by the magnetic length. We can thus approximate $S_{\pm} \simeq R^2 \sum_n |\langle n | \hat{\rho}_{\pm 1} | 0 \rangle|^2$, where $\hat{\rho}_{\ell} = \int e^{i\ell\theta} \hat{\rho}_{\text{eff}}(\theta) d\theta$ is the angular Fourier transform of a one-dimensional edge density, $\hat{\rho}_{\text{eff}}(\theta) = \int \hat{\rho}(\mathbf{r}) r dr$. Following Wen's bosonization [46, 47, 64, 65], we identify $\hat{\rho}_{+\ell} = \sqrt{|C_{\text{MB}}| \ell} \hat{b}_{\ell}^{\dagger}$, with the operator \hat{b}_{ℓ}^{\dagger} creating a bosonic excitation along the edge of the system, and $\hat{\rho}_{-\ell} = \hat{b}_{+\ell}^{\dagger}$ as its annihilation; here we explicitly used the relation between the filling fraction and the many-body Chern number. The ground state $|0\rangle$ is naturally interpreted as the vacuum of bosonic excitations and the excited states $|n\rangle$ as the states that can be obtained from it through the action of \hat{b}_{ℓ}^{\dagger} . Since the edge mode carries a definite chirality, one obtains $S_+ = |C_{\text{MB}}|A/\pi$, while the opposite orientation yields $S_- = 0$. As anticipated, we exactly recover Eqs. (2)-(3), where the sum rule is entirely exhausted by the gapless edge modes. In the presence of multiple edge channels, or

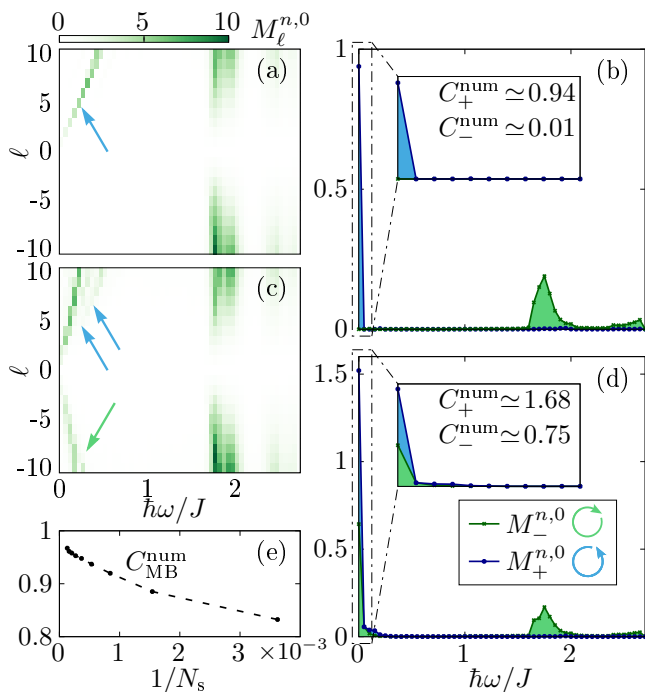


FIG. 2. (a) Angular-momentum-resolved spectroscopy: Matrix elements $M_{\ell}^{n,0} = |\int d^2\mathbf{r} e^{i\ell\theta} \langle n|\hat{\rho}(\mathbf{r})|0\rangle|^2$, as a function of frequency, $\omega_{n,0} = (\varepsilon_n - \varepsilon_0)/\hbar$, and transferred (optical) angular momentum ℓ ; ε_n is the energy of the n th eigenstate. The single chiral gapless branch is indicated by a blue arrow. We set $\phi = 2/7$ and $\varepsilon_F = -1.5J$, considering circular hard walls at $r_{\text{wall}} = 14.5$. (b) CD matrix elements $M_{\pm}^{n,0}$ [Eq. (5)], as a function of $\omega_{n,0}$, with the inset zooming in on the low-energy features. The numerically extracted Chern number contributions, $C_{\text{MB}}^{\text{num}} = C_+^{\text{num}} - C_-^{\text{num}}$, are calculated by isolating the low-energy response ($\hbar\omega \leq 1J$). (c) $C_{\text{MB}}^{\text{num}}$ approaches the quantized value for increasing system size, denoted by the total number of occupied sites, N_s . (d) Same as (a,b) but with multiple edge modes induced by the addition of a ring-shaped potential bump of strength $0.5J$, centered two sites away from the walls [62]. In (b,d), the matrix elements are summed within a small frequency window (of width $0.05J/\hbar$) for visualization.

non-circular boundaries, the result $S_- = 0$ is generally no longer valid. However, the difference $S_+ - S_- = |C_{\text{MB}}|A/\pi$ remains quantized [62], in agreement with Eqs. (2)-(3). In fact, for non-circular boundaries, the ratio S_+/S_- can be used to measure the droplet's anisotropy [62].

Summarizing, we established that a quantized CD edge response is expected at low frequencies [Fig. 1(b,c)]. The bulk gap naturally leads to a frequency separation, which can be exploited to isolate the quantized CD edge response from the bulk one, as we now illustrate by considering realistic models of CI and FCI states.

Model— We consider the Harper-Hofstadter model on a square lattice [8]. In the Landau gauge, the Hamilto-

nian is given by

$$H_0 = -J \sum_{m,n} \left(e^{i2\pi\phi m} a_{m,n+1}^{\dagger} a_{m,n} + a_{m+1,n}^{\dagger} a_{m,n} + \text{h.c.} \right) + H_{\text{int}} + \sum_{m,n} V_{m,n} a_{m,n}^{\dagger} a_{m,n}, \quad (6)$$

which describes particles hopping on a lattice with nearest-neighbour tunneling amplitude J , under the influence of a uniform magnetic field, with a flux ϕ per plaquette. Here, $a_{m,n}^{(\dagger)}$ annihilates (creates) a particle at the lattice site $\mathbf{r}_{m,n} = m\hat{e}_x + n\hat{e}_y$, where we set the lattice constant to unity, and $(m,n) \in \mathbb{Z}$. We also allow for interactions (H_{int}), and an additional confining potential $V_{m,n}$, which will be used to control the edge-mode configuration. We note that trapping potentials can now be finely designed in ultracold atoms, using digital-micromirror or spatial-light-modulator techniques [49].

This model is known to host a plethora of CI and FCI states, depending on the nature of the interactions and particle statistics [66–78]. In the following, we consider CI states of non-interacting fermions and Laughlin-type FCI states of hard-core bosons. For simplicity, we will mostly consider QH states with a single chiral edge mode; however, by engineering the local edge potential $V_{m,n}$, more complicated edge structures and dichroic responses can be obtained, as will be analyzed below.

CI case— We set the flux $\phi = 2/7$ and focus on the CI ground state ($H_{\text{int}} = 0$) with $C_{\text{MB}} = -1$, obtained by fixing the Fermi energy in the first bulk gap ($\varepsilon_F = -1.5J$). Considering a circular confinement with infinite strength ($V_{m,n} \rightarrow \infty$ for $r_{m,n} \geq r_{\text{wall}}$), the system supports a single topological edge mode. In practice, the chiral mode can be revealed by a spectroscopic probe that injects ℓ units of angular momentum in an energy-selective way, as provided by two interfering Laguerre-Gauss beams [79]. We show the corresponding matrix elements M_{ℓ} in Fig. 2(a), where a single low-energy chiral branch, well-separated from higher-frequency bulk responses, is clearly visible.

We now explore the CD response of the CI state in this circular-box geometry. Figure 2(b) displays the coupling matrix elements $M_{\pm}^{n,0}$, defined in Eq. (5), as a function of the frequency $\omega_{n,0} = (\varepsilon_n - \varepsilon_0)/\hbar$, where ε_n denotes the energy of the n th eigenstate. At low frequency, the system strongly responds to the probe with positive chirality, while it remains immune to the opposite orientation, $M_-^{n,0} = 0$. This situation is reversed at larger frequencies, above the bulk gap, where $M_-^{n,0}$ is shown to contribute to the (quantized) bulk response. The χ LL prediction $S_+ = |C_{\text{MB}}|A/\pi$ is verified by integrating the corresponding excitation rates $\Gamma_{\pm}(\omega)$ up to a frequency cut-off ($\hbar\omega \leq 1J$), which isolates the quantized response of the chiral edge mode [62]. The Chern number extracted from this low-energy response is shown to converge to $|C_{\text{MB}}^{\text{num}}| \simeq 1$ in the large-size limit; see Fig. 2(e).

Next, we demonstrate that this quantized low-energy

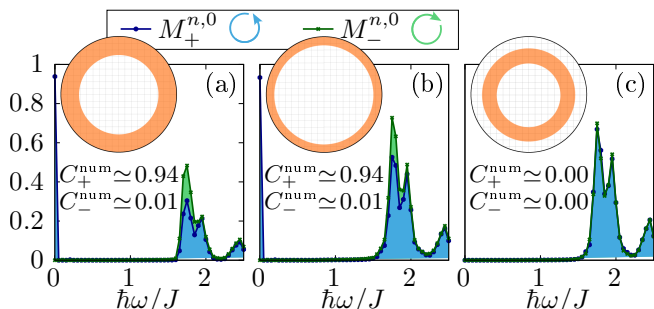


FIG. 3. Matrix elements $M_{\pm}^{n,0}$ for a CD probe that acts locally on an annular region of width w (insets) [62], for the same system parameters [Fig. 2(b)]. The local probe with (a) $w=8$ and (b) $w=4$ couples to the chiral edge mode at low energies. The Chern number $C_{\text{MB}}^{\text{num}}$ extracted from the low-energy response ($\hbar\omega \leq J$) remains quantized. (c) A probe localized deep in the bulk yields a vanishing low-energy CD response.

response is indeed associated with the chiral mode that propagates on the boundary. To do so, we now apply the CD probe locally on the edge using a spatial mask [62]. The corresponding matrix elements and extracted Chern numbers are displayed in Fig. 3(a,b), for two configurations of the probe’s profile, showing robustness of the quantized edge response. We show in Fig. 3(c) that this low-energy response vanishes as soon as the local probe departs from the edge.

Finally, we analyze how multiple (possibly counter-propagating) edge modes can modify the CD response. This situation can be engineered by modifying the shape of the edge potential, e.g. by applying an additional ring-shaped “bump” close to the boundary [62]. Doing so, we obtain a pair of additional branches with opposite chirality, as required by the bulk-edge correspondence [80, 81]. This richer edge structure is confirmed in Fig. 2(c) through angular-momentum-selective spectroscopy. In this case, the low-frequency CD response has contributions from both driving orientations, $M_{\pm} \neq 0$, as we confirm in Fig. 2(d). The Chern number $|C_{\text{MB}}^{\text{num}}|$ is then properly extracted from the differential integrated rates $\Gamma_{+}^{\text{int}} - \Gamma_{-}^{\text{int}}$, upon introducing a low-frequency cutoff that isolates the edge response, hence confirming the χ LL prediction [62].

FCI case— We now consider the bosonic Laughlin state at $\nu=1/2$, hosted by the Harper-Hofstadter model in Eq. (6) with hard-core interactions. Here, we add a weak harmonic potential $V_{m,n}=U_h(m^2+n^2)$, which helps isolating a well-defined branch of edge-modes [50, 69, 82], and stabilizes a Laughlin-like state with an approximately circular edge.

We study the CD response of this FCI state by calculating the coupling matrix elements M_{\pm} ; our results are shown in Fig. 4 as a function of the flux ϕ . In agreement with the χ LL prediction for a single chiral edge mode, we find $M_{+} \neq 0$ and $M_{-} = 0$ at low energy [Fig. 4(a,c)].

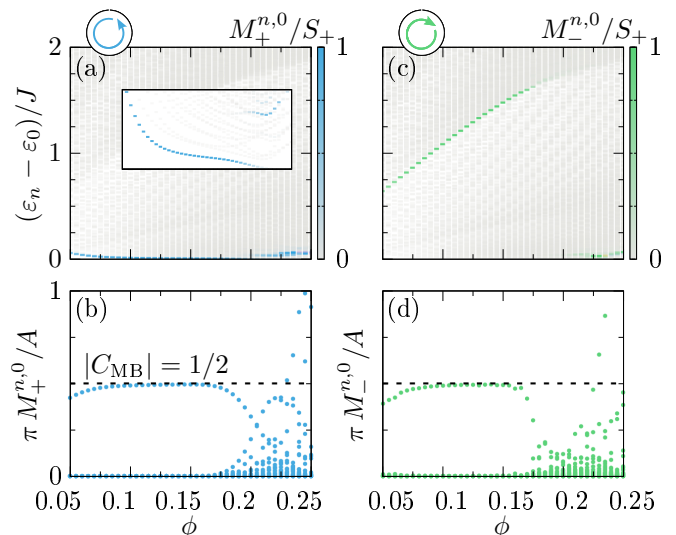


FIG. 4. (a) Energy spectrum for $N=2$ hardcore bosons on a 12×12 square lattice, in the presence of a weak harmonic confinement of strength $U_h = 3.5 \times 10^{-3}J$, as a function of the flux ϕ . The points have been coloured according to the magnitude of the matrix elements $M_{+}^{n,0}$. The inset shows a close-up on the low-energy features. (b) The same matrix elements, without energy resolution, and compared to the theory prediction (black dashed line). (c,d) Same but for the matrix elements $M_{-}^{n,0}$, associated with the bulk response.

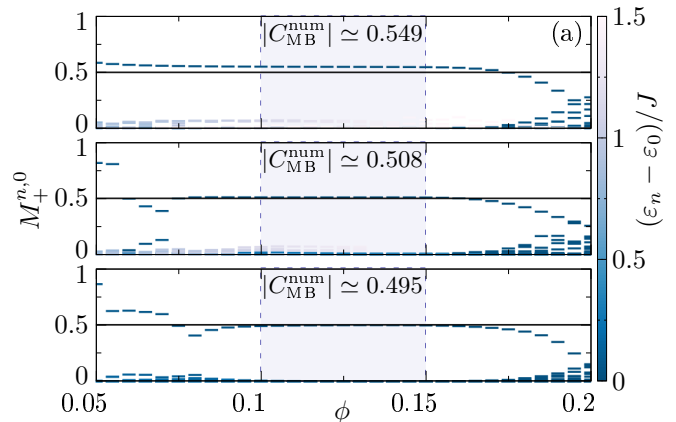


FIG. 5. Matrix elements $M_{+}^{n,0}$ for $f(r)=1$ (see text) as a function of the flux ϕ ; points are coloured according to the energy of the n th state, relative to the ground state. We consider (a) $N=2$, (b) $N=3$ and (c) $N=4$ bosons on a 12×12 lattice, in the presence of a weak harmonic confinement of strength $U_h = 0.002J$. The points are compared with the theoretical prediction $\Delta S = |C_{\text{MB}}|$ (black line). The reported values $|C_{\text{MB}}^{\text{num}}|$ are averages in the blue-shaded region.

Since a single edge mode couples to the CD probe, the corresponding matrix element is directly related to the many-body Chern number $|C_{\text{MB}}| = 1/2$, as we demonstrate in Fig. 4(b). We note that this result can be used to identify the flux window within which the FCI state is stabilized. From Fig. 4(a), we also find that the energy of

the relevant low-energy mode decreases with increasing magnetic flux, as expected from a semiclassical description of the edge mode.

In contrast, the probe with negative orientation couples to a single high-energy (bulk) mode, at the cyclotron energy $\hbar\omega_c \propto \phi$ [Fig. 4(c)]. In accordance with Eq. (3), the corresponding matrix element is also related to the many-body Chern number $|C_{\text{MB}}|$, hence exactly compensating the low-energy edge response. We note that it is the cyclotron gap (and not the many-body gap, which is much smaller) that sets the energy scale at which absorption of opposite angular-momentum quanta occurs.

We finally comment on the possibility of exciting the system with a generalized CD probe described by a time-dependent potential of the form $U_{\pm}(\mathbf{r}, t) = Ef(r)e^{i(\pm\theta - \omega t)} + \text{c.c.}$, where $f(r)$ denotes a general profile function. Since the bulk is incompressible at low-energy, the spatial profile of the probe is irrelevant deep in the bulk ($r \approx 0$). A straightforward generalization of our calculations above [62] yields $\Delta S = \sum_{n \in \text{edge}} (M_+^{n,0} - M_-^{n,0}) = |f(R)|^2 |C_{\text{MB}}|$: While the edge response encodes the many-body Chern number, it is also sensitive to the probe intensity at the edge ($r = R$). In particular, one recovers $\Delta S = |C_{\text{MB}}|A/\pi$ in the case of a uniform circular drive ($f(r) = r$). We explore this idea by choosing a probe with a constant profile, $f(r) = 1$, which has the advantage of providing direct access to the many-body Chern number, without any prior knowledge of the system's size. We note that the probe is unphysical at $r = 0$, but this does not affect the results since the bulk remains inert at low-energy. We display the relevant matrix elements M_{\pm} in Fig. 5, as a function of the flux, for various system sizes. Deep in the FCI region, a single low-energy edge mode is shown to react to the generalized CD probe, and leads to the quantized response $\Delta S \simeq |C_{\text{MB}}|$. As we increase the number of particles, the value $|C_{\text{MB}}^{\text{num}}|$ that we extract from the plateau region saturates towards $|C_{\text{MB}}| = 1/2$. These results indicate how the many-body Chern number of correlated insulators can be directly extracted from the edge response, using a Laguerre-Gaussian-type probe [50, 79].

Concluding remarks—Cold atoms in optical lattices [8] appear as a natural platform to measure the quantized edge response explored in this work: the edge-mode configuration could be finely controlled by adjusting the confining potential [49], and angular-momentum-sensitive spectroscopy could be applied locally on the edge of the cloud, using Laguerre-Gaussian beams [50, 79, 83]. These methods could be directly applied to few-atom FCI states recently realized in experiments [83, 84]. In these settings, the edge spectrum is highly discretized, such that the relevant matrix elements M_{\pm} could be directly extracted from Rabi oscillations [44, 50, 85]. It would be interesting to investigate extensions to non-Abelian topological matter, displaying exotic edge structures [86].

Acknowledgments — The authors thank Iacopo Carusotto, Jean Dalibard, Daniele de Bernardis, Leonardo Mazza, Blagoje Oblak, Cecile Repellin and Peter Zoller for stimulating discussions. F.N.Ü. acknowledges funding from the Marie Skłodowska-Curie programme of the European Commission No 893915, Simons Investigator Award [Grant No. 511029] and Trinity College Cambridge. A. N. thanks financial support from LoCoMacro 805252 from the European Research Council. N. G. is supported by the ERC Grant LATIS and the EOS project CHEQS.

* fnu20@cam.ac.uk

† alberto.nardin@universite-paris-saclay.fr

‡ nathan.goldman@lkb.ens.fr

§ These authors contributed equally to this work.

- [1] S. M. Girvin, The quantum hall effect: Novel excitations and broken symmetries, in *Aspects topologiques de la physique en basse dimension. Topological aspects of low dimensional systems: Session LXIX. 7–31 July 1998* (Springer, 2002) pp. 53–175.
- [2] D. J. Thouless, M. Kohmoto, M. P. Nightingale, and M. den Nijs, Quantized hall conductance in a two-dimensional periodic potential, *Phys. Rev. Lett.* **49**, 405 (1982).
- [3] Q. Niu, D. J. Thouless, and Y.-S. Wu, Quantized hall conductance as a topological invariant, *Phys. Rev. B* **31**, 3372 (1985).
- [4] G. E. Volovik, *The universe in a helium droplet*, Vol. 117 (OUP Oxford, 2003).
- [5] B. A. Bernevig, *Topological insulators and topological superconductors* (Princeton university press, 2013).
- [6] M. Z. Hasan and C. L. Kane, Colloquium: Topological insulators, *Rev. Mod. Phys.* **82**, 3045 (2010).
- [7] X.-L. Qi and S.-C. Zhang, Topological insulators and superconductors, *Rev. Mod. Phys.* **83**, 1057 (2011).
- [8] N. R. Cooper, J. Dalibard, and I. B. Spielman, Topological bands for ultracold atoms, *Rev. Mod. Phys.* **91**, 015005 (2019).
- [9] T. Ozawa, H. M. Price, A. Amo, N. Goldman, M. Hafezi, L. Lu, M. C. Rechtsman, D. Schuster, J. Simon, O. Zilberberg, and I. Carusotto, Topological photonics, *Rev. Mod. Phys.* **91**, 015006 (2019).
- [10] F. Schlawin, D. M. Kennes, and M. A. Sentef, Cavity quantum materials, *Applied Physics Reviews* **9**, 011312 (2022).
- [11] J. Bloch, A. Cavalleri, V. Galitski, M. Hafezi, and A. Rubio, Strongly correlated electron–photon systems, *Nature* **606**, 41 (2022).
- [12] Z. Bacciconi, H. Xavier, I. Carusotto, T. Chanda, and M. Dalmonte, Theory of fractional quantum hall liquids coupled to quantum light and emergent graviton-polaritons, *arXiv preprint arXiv:2405.12292* (2024).
- [13] L. Wu, M. Salehi, N. Koirala, J. Moon, S. Oh, and N. Armitage, Quantized faraday and kerr rotation and axion electrodynamics of a 3d topological insulator, *Science* **354**, 1124 (2016).
- [14] F. De Juan, A. G. Grushin, T. Morimoto, and J. E. Moore, Quantized circular photogalvanic effect in weyl

- semimetals, *Nature communications* **8**, 15995 (2017).
- [15] D. T. Tran, A. Dauphin, A. G. Grushin, P. Zoller, and N. Goldman, Probing topology by heating: Quantized circular dichroism in ultracold atoms, *Science advances* **3**, e1701207 (2017).
- [16] J. Ahn, G.-Y. Guo, N. Nagaosa, and A. Vishwanath, Riemannian geometry of resonant optical responses, *Nature Physics* **18**, 290 (2022).
- [17] A. Kruchkov and S. Ryu, Spectral sum rules reflect topological and quantum-geometric invariants, *arXiv preprint arXiv:2312.17318* (2023).
- [18] I. Souza and D. Vanderbilt, Dichroic f -sum rule and the orbital magnetization of crystals, *Phys. Rev. B* **77**, 054438 (2008).
- [19] T. Morimoto, Y. Hatsugai, and H. Aoki, Optical hall conductivity in ordinary and graphene quantum hall systems, *Phys. Rev. Lett.* **103**, 116803 (2009).
- [20] B. M. Fregoso, R. A. Muniz, and J. E. Sipe, Jerk current: A novel bulk photovoltaic effect, *Phys. Rev. Lett.* **121**, 176604 (2018).
- [21] A. Bouhon, A. Timmel, and R.-J. Slager, Quantum geometry beyond projective single bands, *arXiv preprint arXiv:2303.02180* (2023).
- [22] Y. Onishi and L. Fu, Fundamental bound on topological gap, *Physical Review X* **14**, 011052 (2024).
- [23] W. J. Jankowski, A. S. Morris, A. Bouhon, F. N. Ünal, and R.-J. Slager, Optical manifestations of topological euler class in electronic materials, *arXiv preprint arXiv:2311.07545* (2023).
- [24] T. Ozawa and N. Goldman, Extracting the quantum metric tensor through periodic driving, *Phys. Rev. B* **97**, 201117 (2018).
- [25] C. Repellin and N. Goldman, Detecting fractional chern insulators through circular dichroism, *Phys. Rev. Lett.* **122**, 166801 (2019).
- [26] P. W. Klein, A. G. Grushin, and K. Le Hur, Interacting stochastic topology and mott transition from light response, *Phys. Rev. B* **103**, 035114 (2021).
- [27] K. Le Hur, Global and local topological quantized responses from geometry, light, and time, *Phys. Rev. B* **105**, 125106 (2022).
- [28] O. Pozo, C. Repellin, and A. G. Grushin, Quantization in chiral higher order topological insulators: Circular dichroism and local chern marker, *Phys. Rev. Lett.* **123**, 247401 (2019).
- [29] T. Ozawa and N. Goldman, Probing localization and quantum geometry by spectroscopy, *Phys. Rev. Res.* **1**, 032019 (2019).
- [30] M. Schüler, U. De Giovannini, H. Hübener, A. Rubio, M. A. Sentef, T. P. Devereaux, and P. Werner, How circular dichroism in time- and angle-resolved photoemission can be used to spectroscopically detect transient topological states in graphene, *Phys. Rev. X* **10**, 041013 (2020).
- [31] M. Schüler, U. De Giovannini, H. Hübener, A. Rubio, M. A. Sentef, and P. Werner, Local berry curvature signatures in dichroic angle-resolved photoelectron spectroscopy from two-dimensional materials, *Science advances* **6**, eaay2730 (2020).
- [32] R. L. Klees, G. Rastelli, J. C. Cuevas, and W. Belzig, Microwave spectroscopy reveals the quantum geometric tensor of topological josephson matter, *Phys. Rev. Lett.* **124**, 197002 (2020).
- [33] P. Mognini, B. Lapierre, R. Chitra, and W. Chen, Probing Chern number by opacity and topological phase transition by a nonlocal Chern marker, *SciPost Phys. Core* **6**, 059 (2023).
- [34] N. Goldman and T. Ozawa, Relating the hall conductivity to the many-body chern number using fermi's golden rule and kramers-kronig relations, *arXiv preprint arXiv:2403.03340* (2024).
- [35] J. Kim, D. Kim, D. E. Kim, and A. Chacón, Circular dichroism in floquet chern insulator via high-order harmonics spectroscopy, *Journal of Physics: Condensed Matter* **36**, 035701 (2023).
- [36] L. Asteria, D. Tran, T. Ozawa, M. Tarnowski, B. S. Rem, N. Flashner, K. Sengstock, N. Goldman, and C. Weitenberg, Measuring quantized circular dichroism in ultracold topological matter, *Nat. Phys* **15**, 449 (2019).
- [37] M. Yu, P. Yang, M. Gong, Q. Cao, Q. Lu, H. Liu, S. Zhang, M. B. Plenio, F. Jelezko, T. Ozawa, *et al.*, Experimental measurement of the quantum geometric tensor using coupled qubits in diamond, *National Science Review* **7**, 254 (2020).
- [38] X. Tan, D.-W. Zhang, Z. Yang, J. Chu, Y.-Q. Zhu, D. Li, X. Yang, S. Song, Z. Han, Z. Li, Y. Dong, H.-F. Yu, H. Yan, S.-L. Zhu, and Y. Yu, Experimental measurement of the quantum metric tensor and related topological phase transition with a superconducting qubit, *Phys. Rev. Lett.* **122**, 210401 (2019).
- [39] M. Yu, Y. Liu, P. Yang, M. Gong, Q. Cao, S. Zhang, H. Liu, M. Heyl, T. Ozawa, N. Goldman, *et al.*, Quantum fisher information measurement and verification of the quantum cramer-rao bound in a solid-state qubit, *npj Quantum Information* **8**, 56 (2022).
- [40] M. Yu, X. Li, Y. Chu, B. Mera, F. N. Ünal, P. Yang, Y. Liu, N. Goldman, and J. Cai, Experimental demonstration of topological bounds in quantum metrology, *National Science Review* , nwae065 (2024).
- [41] M. Chen, C. Li, G. Palumbo, Y.-Q. Zhu, N. Goldman, and P. Cappellaro, A synthetic monopole source of kalbramond field in diamond, *Science* **375**, 1017 (2022).
- [42] X. Tan, D.-W. Zhang, W. Zheng, X. Yang, S. Song, Z. Han, Y. Dong, Z. Wang, D. Lan, H. Yan, S.-L. Zhu, and Y. Yu, Experimental observation of tensor monopoles with a superconducting qudit, *Phys. Rev. Lett.* **126**, 017702 (2021).
- [43] I. Souza and D. Vanderbilt, Dichroic f -sum rule and the orbital magnetization of crystals, *Phys. Rev. B* **77**, 054438 (2008).
- [44] D. T. Tran, N. R. Cooper, and N. Goldman, Quantized rabi oscillations and circular dichroism in quantum hall systems, *Phys. Rev. A* **97**, 061602 (2018).
- [45] X. G. Wen, Electrodynamical properties of gapless edge excitations in the fractional quantum hall states, *Phys. Rev. Lett.* **64**, 2206 (1990).
- [46] X. G. Wen, Chiral luttinger liquid and the edge excitations in the fractional quantum hall states, *Phys. Rev. B* **41**, 12838 (1990).
- [47] X.-G. Wen, Topological orders and edge excitations in fractional quantum Hall states, *Adv. Phys.* **44**, 405 (1995), *arXiv:cond-mat/9506066*.
- [48] A. M. Chang, Chiral luttinger liquids at the fractional quantum hall edge, *Rev. Mod. Phys.* **75**, 1449 (2003).
- [49] N. Navon, R. P. Smith, and Z. Hadzibabic, Quantum gases in optical boxes, *Nature Physics* **17**, 1334 (2021).
- [50] F. Binanti, N. Goldman, and C. Repellin, Spectroscopy

- of edge and bulk collective modes in fractional chern insulators, *Phys. Rev. Res.* **6**, L012054 (2024).
- [51] H. S. Bennett and E. A. Stern, Faraday effect in solids, *Phys. Rev.* **137**, A448 (1965).
- [52] R. Bianco and R. Resta, Mapping topological order in coordinate space, *Phys. Rev. B* **84**, 241106 (2011).
- [53] K. v. Klitzing, G. Dorda, and M. Pepper, New method for high-accuracy determination of the fine-structure constant based on quantized hall resistance, *Phys. Rev. Lett.* **45**, 494 (1980).
- [54] R. B. Laughlin, Quantized hall conductivity in two dimensions, *Phys. Rev. B* **23**, 5632 (1981).
- [55] R. B. Laughlin, Anomalous quantum hall effect: An incompressible quantum fluid with fractionally charged excitations, *Phys. Rev. Lett.* **50**, 1395 (1983).
- [56] B. Oblak, B. Lapiere, P. Moosavi, J.-M. Stéphan, and B. Estienne, Anisotropic quantum hall droplets, *Phys. Rev. X* **14**, 011030 (2024).
- [57] F. D. M. Haldane, Fractional quantization of the hall effect: A hierarchy of incompressible quantum fluid states, *Phys. Rev. Lett.* **51**, 605 (1983).
- [58] B. I. Halperin, Theory of the quantized Hall conductance, *Helv. Phys. Acta* **56**, 75 (1983).
- [59] X. Wan, K. Yang, and E. H. Rezayi, Reconstruction of fractional quantum hall edges, *Phys. Rev. Lett.* **88**, 056802 (2002).
- [60] X. Wan, E. H. Rezayi, and K. Yang, Edge reconstruction in the fractional quantum hall regime, *Phys. Rev. B* **68**, 125307 (2003).
- [61] K. Yang, Field theoretical description of quantum hall edge reconstruction, *Phys. Rev. Lett.* **91**, 036802 (2003).
- [62] See Supplemental Material (SM) for details.
- [63] D. M. Stamper-Kurn and W. Ketterle, Spinor condensates and light scattering from bose-einstein condensates, in *Coherent atomic matter waves: 27 July–27 August 1999* (Springer, 2002) pp. 139–217.
- [64] A. Nardin and I. Carusotto, Linear and nonlinear edge dynamics of trapped fractional quantum hall droplets, *Phys. Rev. A* **107**, 033320 (2023).
- [65] A. Nardin and I. Carusotto, *Refermionized theory of the edge modes of a fractional quantum hall cloud* (2023).
- [66] A. S. Sørensen, E. Demler, and M. D. Lukin, Fractional quantum hall states of atoms in optical lattices, *Phys. Rev. Lett.* **94**, 086803 (2005).
- [67] M. Hafezi, A. S. Sørensen, E. Demler, and M. D. Lukin, Fractional quantum hall effect in optical lattices, *Phys. Rev. A* **76**, 023613 (2007).
- [68] R. N. Palmer, A. Klein, and D. Jaksch, Optical lattice quantum hall effect, *Phys. Rev. A* **78**, 013609 (2008).
- [69] J. A. Kjäll and J. E. Moore, Edge excitations of bosonic fractional quantum hall phases in optical lattices, *Phys. Rev. B* **85**, 235137 (2012).
- [70] G. Möller and N. R. Cooper, Composite fermion theory for bosonic quantum hall states on lattices, *Physical review letters* **103**, 105303 (2009).
- [71] T. Scaffidi and S. H. Simon, Exact solutions of fractional chern insulators: Interacting particles in the hofstadter model at finite size, *Phys. Rev. B* **90**, 115132 (2014).
- [72] D. Bauer, T. S. Jackson, and R. Roy, Quantum geometry and stability of the fractional quantum hall effect in the hofstadter model, *Phys. Rev. B* **93**, 235133 (2016).
- [73] G. Möller and N. R. Cooper, Fractional chern insulators in harper-hofstadter bands with higher chern number, *Phys. Rev. Lett.* **115**, 126401 (2015).
- [74] G. Murthy, Composite fermion hofstadter problem: Partially polarized density wave states in the $\nu = 2/5$ fractional quantum hall effect, *Phys. Rev. Lett.* **84**, 350 (2000).
- [75] M. Račiūnas, F. N. Ünal, E. Anisimovas, and A. Eckardt, Creating, probing, and manipulating fractionally charged excitations of fractional chern insulators in optical lattices, *Phys. Rev. A* **98**, 063621 (2018).
- [76] C. Repellin, J. Léonard, and N. Goldman, Fractional chern insulators of few bosons in a box: Hall plateaus from center-of-mass drifts and density profiles, *Phys. Rev. A* **102**, 063316 (2020).
- [77] F. A. Palm, M. Buser, J. Léonard, M. Aidelsburger, U. Schollwöck, and F. Grusdt, Bosonic pfaffian state in the hofstadter-bose-hubbard model, *Phys. Rev. B* **103**, L161101 (2021).
- [78] J. Boesl, R. Dilip, F. Pollmann, and M. Knap, Characterizing fractional topological phases of lattice bosons near the first mott lobe, *Phys. Rev. B* **105**, 075135 (2022).
- [79] N. Goldman, J. Beugnon, and F. Gerbier, Detecting chiral edge states in the hofstadter optical lattice, *Phys. Rev. Lett.* **108**, 255303 (2012).
- [80] Y. Hatsugai, Edge states in the integer quantum hall effect and the riemann surface of the bloch function, *Phys. Rev. B* **48**, 11851 (1993).
- [81] Y. Hatsugai, Chern number and edge states in the integer quantum hall effect, *Phys. Rev. Lett.* **71**, 3697 (1993).
- [82] W.-W. Luo, W.-C. Chen, Y.-F. Wang, and C.-D. Gong, Edge excitations in fractional chern insulators, *Phys. Rev. B* **88**, 161109 (2013).
- [83] P. Lunt, P. Hill, J. Reiter, P. M. Preiss, M. Galka, and S. Jochim, Realization of a laughlin state of two rapidly rotating fermions, *arXiv preprint arXiv:2402.14814* (2024).
- [84] J. Léonard, S. Kim, J. Kwan, P. Segura, F. Grusdt, C. Repellin, N. Goldman, and M. Greiner, Realization of a fractional quantum hall state with ultracold atoms, *Nature* **619**, 495 (2023).
- [85] A. Nardin, D. De Bernardis, M. Rizzi, R. Umucalilar, L. Mazza, and I. Carusotto, Quantum nonlinear optics on the edge of small lattice fractional quantum hall fluids, *arXiv preprint arXiv:2403.10598* (2024).
- [86] Y. Zhang, G. J. Sreejith, and J. K. Jain, Creating and manipulating non-abelian anyons in cold atom systems using auxiliary bosons, *Phys. Rev. B* **92**, 075116 (2015).
- [87] T. H. Hansson, M. Hermanns, S. H. Simon, and S. F. Viefers, Quantum hall physics: Hierarchies and conformal field theory techniques, *Rev. Mod. Phys.* **89**, 025005 (2017).
- [88] N. R. Cooper, F. J. M. van Lankvelt, J. W. Reijnders, and K. Schoutens, Quantum hall states of atomic bose gases: Density profiles in single-layer and multilayer geometries, *Phys. Rev. A* **72**, 063622 (2005).
- [89] R. J. Fletcher, A. Shaffer, C. C. Wilson, P. B. Patel, Z. Yan, V. Crépel, B. Mukherjee, and M. W. Zwierlein, Geometric squeezing into the lowest landau level, *Science* **372**, 1318 (2021).

NUMERICAL CALCULATIONS

This Appendix provides more details on the numerical calculations presented in Figs. 2 and 3 in the main text. For the CI case, we consider the Harper-Hofstadter model with $\phi = 2/7$ -flux per plaquette confined by hard walls in a circular box of radius r_{wall} with the Fermi energy $\varepsilon_F = -1.5J$ lying in the first bulk gap. To extract the Chern number contributions from the matrix elements $M_{\pm}^{n,0}$ numerically calculated between the eigenstates (see Fig.2b), one needs to factor in the area A of the system carefully. For the circular box potential (Fig. 2b) this is given by the total area $A = \pi r_{\text{wall}}^2$. Figures 2(c,d) however include a modified confining potential to generate additional edge modes of opposite chirality. Specifically, we employ a Gaussian potential of the form $V_0 \exp\{-(\mathbf{r} - \mathbf{r}_0)^2/2\sigma_0^2\}$, centered close to the hard-wall edge at $r_0 = r_{\text{wall}} - 2$ with width $\sigma_0 = 0.5$. This Gaussian potential bump naturally alters the system area since the ground state density indeed depletes in this bump region. We factor this in by considering $A = \pi r_{\text{wall}}^2 - A_{\text{bump}}$, where $A_{\text{bump}} = \int d^2\mathbf{r} \exp\{-(\mathbf{r} - \mathbf{r}_0)^2/2\sigma_0^2\}$ in Fig. 2d.

In Fig. 3, the CI state is confined in a circular box only, with no additional Gaussian bump potential. The CD probe is then applied with a spatial mask with a Heavyside-step profile. In Fig. 3(a) and (b), the probe is considered locally acting on an edge region for $r_{\text{wall}} - 8 \leq r \leq r_{\text{wall}}$ and $r_{\text{wall}} - 4 \leq r \leq r_{\text{wall}}$, respectively. In Fig 3c, the probe is instead localized in the bulk with $r_{\text{wall}} - 13 \leq r \leq r_{\text{wall}} - 5$. We emphasise that in all cases considered in Fig. 3, the numerically extracted Chern number contributions are calculated by using the full system area $A = \pi r_{\text{wall}}^2$ as it relates to the Chern insulating ground state independently from the area targeted by the probe.

QUANTIZED CIRCULAR DICHROISM: EXCITATION RATES AND CONNECTION TO THE HALL CONDUCTIVITY

In this Appendix, we briefly review some of the key concepts at the basis of the circular dichroism. We begin by introducing the conductivity tensor for quantum Hall systems. We then review the connection between the power absorbed by a circularly polarized electric field and the conductivity tensor. We highlight the connection with quantum mechanical rates. We will take advantage of the context to introduce in a more extensive manner the relevant quantities used in the main text and the notation employed therein.

The discussion here is mostly a re-elaboration of Refs. [15, 34, 51].

Conductivity tensor

When an electric field $\mathbf{E}(\mathbf{r}, t)$ is applied to a 2D material, within linear response, a current will flow proportional to the applied field. The current density $J_i(\mathbf{r}, t)$ can be written as

$$J_i(\mathbf{r}, t) = \int d^2\mathbf{r}' \int dt' \sum_j \sigma_{ij}(\mathbf{r} - \mathbf{r}', t - t') E_j(\mathbf{r}', t'). \quad (\text{S1})$$

σ_{ij} is called the conductivity tensor, and under the assumption of isotropy and time-independence it can only depend on relative space-time displacements and must take the general form

$$\sigma = \begin{pmatrix} \sigma_{xx} & \sigma_{xy} \\ -\sigma_{xy} & \sigma_{xx} \end{pmatrix}. \quad (\text{S2})$$

We here introduce our Fourier conventions

$$\begin{aligned} \tilde{E}_i(\mathbf{k}, \omega) &= \frac{1}{(2\pi)^3} \int d^2\mathbf{r} \int dt e^{-i(\mathbf{k}\cdot\mathbf{r} - \omega t)} E_i(\mathbf{r}, t), \\ E_i(\mathbf{r}, t) &= \int d^2\mathbf{k} \int d\omega e^{i(\mathbf{k}\cdot\mathbf{r} - \omega t)} \tilde{E}_i(\mathbf{k}, \omega), \end{aligned} \quad (\text{S3})$$

in terms of which one can write Eq. (S1) as a completely local relation in frequency-momentum space

$$\tilde{J}_i(\mathbf{k}, \omega) = (2\pi)^3 \sum_j \tilde{\sigma}_{ij}(\mathbf{k}, \omega) \tilde{E}_j(\mathbf{k}, \omega). \quad (\text{S4})$$

In the quantum Hall regime (in the bulk), at very long wavelengths, the current response is purely transverse and local, and quantized in terms of the many-body Chern number C_{MB} . Namely,

$$\sigma_{ij}(\mathbf{r} - \mathbf{r}', t - t') = -\frac{q^2}{h} C_{\text{MB}} \epsilon_{ij} \delta(t - t') \delta(\mathbf{r} - \mathbf{r}'), \quad (\text{S5})$$

with ϵ_{ij} a totally antisymmetric tensor and q denotes the charge of the carriers. From Eq. (S1), one recovers the familiar quantized transverse response

$$J_i(\mathbf{r}, t) = -\frac{q^2}{h} C_{\text{MB}} \sum_j \epsilon_{ij} E_j(\mathbf{r}, t). \quad (\text{S6})$$

The Fourier transform of the conductivity tensor therefore reads, with the conventions we adopted,

$$\tilde{\sigma}_{ij}(\mathbf{k}, \omega) = -\frac{1}{(2\pi)^3} \frac{q^2}{h} C_{\text{MB}} \epsilon_{ij}. \quad (\text{S7})$$

Circular dichroism

We here consider a monochromatic, uniform and circularly polarized electric field $\mathbf{E} = \mathbf{E}_{\pm}$ given by

$$\mathbf{E}_{\pm}(\mathbf{r}, t) = 2E e^{-i\omega t} (\hat{e}_x \pm i\hat{e}_y), \quad (\text{S8})$$

impinging on a 2D material in the $x - y$ plane, of area A . For convenience, we use the complex electric field framework [51]; the physical electric field is the real part of \mathbf{E}_\pm , and can be seen to equal $Ee^{-i\omega t}(\hat{e}_x \pm i\hat{e}_y) + \text{c.c.}$, i.e. the same electric field that we introduced in the main text. For notational convenience we also introduce

$$\hat{e}_\pm = \hat{e}_x \pm i\hat{e}_y. \quad (\text{S9})$$

The electric field of Eq. (S8) enters the Schrödinger equation through an additional scalar potential of the form $U_\pm(\mathbf{r}, t) = -2qE(x \cos(\omega t) \pm y \sin(\omega t))$, or, equivalently, in the form of an additional vector potential $\mathbf{A}_\pm(\mathbf{r}, t) = \frac{2E}{\omega}(\sin(\omega t)\hat{e}_x \mp \cos(\omega t)\hat{e}_y)$. In this article, we generally adopt the first approach. We note that such a circular drive can also be implemented in cold-atom setups through a circular shaking of the optical lattice [36].

The time-averaged (over a period $2\pi/\omega$) power absorbed by the material,

$$P_\pm(\omega) = \int d^2\mathbf{r} \overline{\Re \mathbf{J} \cdot \Re \mathbf{E}_\pm} = \frac{1}{2} \Re \int d^2\mathbf{r} \mathbf{J} \cdot \mathbf{E}_\pm^*, \quad (\text{S10})$$

can be related to the conductivity tensor Eq. (S2) by using the current density expression Eq. (S1); after few algebraic manipulations one obtains

$$P_\pm(\omega) = (2\pi)^3 4E^2 A (\tilde{\sigma}_{xx}^R(\omega) \mp \tilde{\sigma}_{xy}^I(\omega)). \quad (\text{S11})$$

Here, $\tilde{\sigma}_{ij}(\omega) = \tilde{\sigma}_{ij}(\mathbf{k} = 0, \omega)$ and the $R(I)$ superscript indicate the real(imaginary) part. Importantly the transverse part of the conductivity tensor, σ_{xy} , is related to circular dichroism: the power absorbed P_\pm associated with opposite circular polarizations \hat{e}_\pm can be different. By taking the difference one indeed obtains a non-zero result,

$$\Delta P(\omega) = -8(2\pi)^3 E^2 A \tilde{\sigma}_{xy}^I(\mathbf{k} = 0, \omega). \quad (\text{S12})$$

In an isotropic system $\sigma_{ij}(\mathbf{r}, t) = \sigma_{ij}(-\mathbf{r}, t)$ the real and imaginary parts of the conductivity tensor can be related by the famous Kramers-Kronig relations,

$$\tilde{\sigma}_{xy}^R(\omega) = \frac{2}{\pi} \int_0^\infty \frac{\omega' \tilde{\sigma}_{xy}^I(\omega')}{(\omega')^2 - \omega^2} d\omega', \quad (\text{S13})$$

which, in the $\omega \rightarrow 0$ limit, yield a sum-rule through which one relates the circular dichroism in Eq. (S12) to the Hall transverse response,

$$\frac{2}{\pi} \int_0^\infty \frac{\Delta P(\omega)}{\omega} d\omega = -8(2\pi)^3 E^2 A \tilde{\sigma}_{xy}^R(0). \quad (\text{S14})$$

Connection to quantum mechanical rates

The absorbed power can be related to quantum-mechanical rates: Since the absorbed power at the given

frequency is the energy absorbed per unit time, and the energy is absorbed in quanta $\hbar\omega$, we can write

$$\frac{P_\pm(\omega)}{\hbar\omega} = \Gamma_\pm(\omega), \quad (\text{S15})$$

where $\Gamma_\pm(\omega)$ is the transition rate from the system's ground state $|0\rangle$ to any other state. We point out that the rate difference $\Delta\Gamma(\omega) = \Gamma_+(\omega) - \Gamma_-(\omega)$ is the quantity that appears in the left hand side of Eq. (S14).

The rates can be computed within the scope of perturbation theory. One can indeed see the impinging electric field Eq. (S8) as a time-dependent external potential,

$$U_\pm(\mathbf{r}, t) = \Re[-2qEe^{-i\omega t}(x \pm iy)], \quad (\text{S16})$$

being applied to the system. Using Fermi's golden rule one obtains

$$\Gamma_\pm(\omega > 0) = 4\pi \frac{q^2 E^2}{\hbar^2} \sum_n M_\pm^{n,0} \delta(\omega - \omega_{n,0}). \quad (\text{S17})$$

Here, $\omega_{n,0} = \frac{\varepsilon_n - \varepsilon_0}{\hbar} \geq 0$ are the (many-body) Bohr's frequencies and the matrix elements $M_\pm^{n,0}$ are the same as those we introduced in the main text in Eq. (5), namely

$$M_\pm^{n,0} = \left| \int (x \pm iy) \langle n | \hat{\rho}(\mathbf{r}) | 0 \rangle d^2\mathbf{r} \right|^2, \quad (\text{S18})$$

with $\hat{\rho}(\mathbf{r}) = \sum_{j=1}^N \delta^{(2)}(\mathbf{r}_i - \mathbf{r}_j)$ being the particle density operator.

When, in the spirit of Eq. (S14), the rates are integrated over all the (positive) frequencies, one obtains

$$\Gamma_\pm^{\text{int}} = \int_0^\infty \Delta\Gamma(\omega) d\omega = 4\pi \frac{q^2 E^2}{\hbar^2} S_\pm, \quad (\text{S19})$$

$$S_\pm = \sum_n M_\pm^{n,0}. \quad (\text{S20})$$

These equations link the frequency integrated transition rates Γ_\pm^{int} to the summation of all the possible transition matrix-elements, $S_\pm = \sum_n M_\pm^{n,0}$.

Using this result in conjunction with Eq. (S14), we can write

$$\frac{\hbar^2}{2q^2 E^2 A} (\Gamma_+^{\text{int}} - \Gamma_-^{\text{int}}) = -(2\pi)^3 \frac{\tilde{\sigma}_{xy}^R(0)}{q^2/h}. \quad (\text{S21})$$

If the system is infinite (pure bulk), then $\tilde{\sigma}_{xy}^R(0)$ is given by Eq. (S7), yielding

$$\frac{\hbar^2}{2q^2 E^2 A} (\Gamma_+^{\text{int}} - \Gamma_-^{\text{int}})_{\text{bulk}} = +C_{\text{MB}}, \quad (\text{S22})$$

which is the same formula we quoted in the main text [see Eq. (2)], when setting the charge $q=1$.

Importantly, if the system is finite, then no net current can be present at any time. Namely, it must hold true that

$$\int J_i(\mathbf{r}, t) d^2\mathbf{r} = 0. \quad (\text{S23})$$

This, together with Eq. (S2), implies that $\int \sigma_{ij}(\mathbf{r} - \mathbf{r}, t) d^2\mathbf{r} = 0$, since the applied electric field is generic. Equivalently,

$$\tilde{\sigma}_{ij}(\mathbf{k} = 0, \omega) = 0, \quad (\text{S24})$$

which implies (see Eq. (S21)) that

$$\frac{\hbar^2}{2q^2 E^2 A} (\Gamma_+^{\text{int}} - \Gamma_-^{\text{int}}) = 0. \quad (\text{S25})$$

This means that the frequency integrated transition rates for a clockwise and anticlockwise polarized electric field exactly cancel out.

Expressed differently, one can state that the bulk dichroic response given by Eq. (S22) must be exactly canceled by a second contribution, which must originate from the presence of an edge in a finite system; namely,

$$(\Gamma_+^{\text{int}} - \Gamma_-^{\text{int}})_{\text{bulk}} = -(\Gamma_+^{\text{int}} - \Gamma_-^{\text{int}})_{\text{edge}}, \quad (\text{S26})$$

as we discussed in the main text; see Eq. (3).

QUANTIZED CIRCULAR-DICHOIC RESPONSE OF EDGE MODES

Here, we provide a more detailed derivation of the low-energy dichroic response, obtained from the viewpoint of the χ LL theory, which is sketched in the main text. We also take this opportunity to present two natural extensions, considering situations involving multiple edge-mode branches, and QH droplets with non-circular geometry.

First, we will assume that the fractional quantum Hall liquid has an approximately circular shape, with constant density throughout $\rho_0 = \nu/(2\pi l_B^2)$, occupying an area πR^2 , with $R = \sqrt{2N/\nu} l_B$. Here $\nu = -C_{\text{MB}}$ is the (fractionally) quantized filling fraction of the system and $l_B = \sqrt{\hbar/qB}$ the magnetic length.

In the following, we will thus be computing S_{\pm} [see Eq. (5)] from a low-energy perspective. For the sake of generality, we will be considering a perturbing potential of the form $U_{\pm}(\mathbf{r}, t) = -qE(f(r)e^{i(\pm\theta - \omega t)} + \text{c.c.})$ which has an arbitrary radial profile $f(r)$ but still carries one unit of angular momentum. The relevant matrix elements [compare to Eq. (S19)] then read

$$S_{\pm} = \sum_{n \in \text{edge}} |v_{\pm}^{n,0}|^2, \quad (\text{S27})$$

$$v_{\pm}^{n,0} = \int f(r) e^{\pm i\theta} \langle n | \hat{\rho}(\mathbf{r}) | 0 \rangle d\mathbf{r}, \quad (\text{S28})$$

which generalize those presented in Eq. (5) for the more standard circular-dichroic setting (i.e. a uniform circularly-polarized electric field). Contrary to Eq. (S19),

here the summation is taken over the low-energy edge-modes only, so as to isolate the edge contribution from the bulk one.

Since the bulk is incompressible, contributions to the integral appearing in Eq. (S28) can only come from the edge region, located at $r \simeq R$, with a typical width set by the magnetic length l_B . As a consequence, one can approximate

$$v_{\pm}^{n,0} = f(R) \int d\theta e^{\pm i\theta} \langle n | \hat{\rho}_{\text{eff}}(\theta) | 0 \rangle, \quad (\text{S29})$$

where

$$\hat{\rho}_{\text{eff}}(\theta) = \int \rho(\mathbf{r}) r dr, \quad (\text{S30})$$

is a one-dimensional (edge) density operator obtained by integrating out the direction orthogonal to the edge. As $R \rightarrow \infty$, i.e. when the number of particles N is large, the approximation becomes more and more accurate provided $f(r)$ varies slowly over the edge width $\propto l_B$.

We now recognize the $\ell = \pm 1$ Fourier components

$$\hat{\rho}_{\ell} = \int d\theta e^{i\ell\theta} \hat{\rho}_{\text{eff}}(\theta),$$

of the edge density operator, and rewrite Eq. (S29) as

$$v_{\pm}^{n,0} = f(R) \langle n | \hat{\rho}_{\pm 1} | 0 \rangle. \quad (\text{S31})$$

In the following, we will first discuss the simplest case of a single edge-mode, and then discuss the case of multiple edges.

The case of a single edge

Following Wen [47, 87], the excess density along the edge of a QH droplet fails to commute, and leads to a $U(1)$ Kac-Moody algebra,

$$[\hat{\rho}_{\ell}, \hat{\rho}_{\ell'}] = \nu \ell \delta_{\ell, -\ell'}. \quad (\text{S32})$$

As previously, ν represents the (fractionally quantized) filling fraction defined in the bulk of the QH droplet, and it naturally comes into play through the average bulk density, $\rho_0 = \nu/(2\pi l_B^2)$.

As a consequence of Eq. (S32), the operators $\hat{\rho}_{\ell}$ can be identified as bosonic annihilation (/creation) operators

$$\begin{cases} \hat{\rho}_{\ell > 0} = \sqrt{\nu|\ell|} \hat{b}_{\ell}^{\dagger} \\ \hat{\rho}_{\ell < 0} = \sqrt{\nu|\ell|} \hat{b}_{\ell}, \end{cases} \quad (\text{S33})$$

$$[\hat{b}_{\ell}, \hat{b}_{\ell'}^{\dagger}] = \delta_{\ell, \ell'}. \quad (\text{S34})$$

The ground state $|0\rangle$ is identified as the vacuum of bosonic excitations, while the excited states are obtained by acting on it with the creation operators \hat{b}_{ℓ}^{\dagger} .

It follows immediately that, for every possible edge state $|n\rangle$, the matrix elements $v_-^{n,0} = 0$ entering Eq. (S31) must vanish. The ground state $|0\rangle$ is indeed annihilated by $\hat{\rho}_{-1}$; it follows that $S_- = 0$. This can be easily seen as a consequence of the presence of a single chiral edge mode: $\hat{\rho}_{-1}$ aims at lowering the ground state angular momentum, but there is no gapless edge mode (with the corresponding angular momentum) that can be excited.

Therefore, in the case of a single chiral branch of edge modes, only $v_+^{n,0}$ can be non-zero. By inspection of Eqs. (S31)- (S33) it is straightforward to realize that the only state contributing to the sum in Eq. (S27) is $|1\rangle = \hat{b}_1^\dagger |0\rangle$, and thus

$$S_+ = v_+^{1,0} = |f(R)|^2 \nu. \quad (\text{S35})$$

By identifying the quantized filling fraction ν with the many-body Chern number, $\nu = -C_{\text{MB}}$, the previous equation can equivalently be written as

$$S_+ - S_- = S_+ = |f(R)|^2 |C_{\text{MB}}|. \quad (\text{S36})$$

In the conventional circular-dichroism case (uniform circular drive), $f(R) = R$ and the result can be rewritten as

$$S_+ - S_- = \frac{A}{\pi} |C_{\text{MB}}|, \quad (\text{S37})$$

which is the result quoted in the main text.

The case of multiple edges

Considering the case of multiple (spatially separated) edges, potentially displaying modes of different nature, S_- can now be finite. Indeed, in this case, the action of $\hat{\rho}_{\ell < 0}$ on the ground state can be non-trivial and contribute to the total excitation rate.

When multiple edge modes are present, the effective one-dimensional edge density $\hat{\rho}_{\text{eff}}(\theta)$ can be split into several density operators, each associated with a different edge channel,

$$\hat{\rho}_{\text{eff}}(\theta) = \sum_e \hat{\rho}_e(\theta). \quad (\text{S38})$$

Here, the sum runs over all the edge modes and $\hat{\rho}_e(\theta)$ is the density operator associated to a given channel. It is useful to introduce the Fourier transform of each component $\hat{\rho}_e(\theta)$ as

$$\hat{\rho}_{e,\ell} = \int d\theta e^{i\ell\theta} \hat{\rho}_e(\theta). \quad (\text{S39})$$

Analogously to Eq. (S33), these operators fail to commute. When the edges are well separated (by a distance much larger than the magnetic length l_B), they satisfy [47]

$$[\hat{\rho}_{e,\ell}, \hat{\rho}_{e',\ell'}] = \nu_e \delta_{e,e'} \delta_{\ell,-\ell'}. \quad (\text{S40})$$

Here ν_e is the (signed) difference between the filling fractions of the fluids sitting on the opposite sides of the edge, the vacuum corresponding to zero filling. As a consequence, these numbers fulfill the constraint $\sum_e \nu_e = \nu$, where ν is the bulk filling fraction, i.e. the many-body Chern number.

As a consequence of Eq. (S40), provided $\nu_e > 0$, one can introduce bosonic operators as

$$\begin{cases} \hat{\rho}_{e,\ell > 0} &= \sqrt{\nu_e |\ell|} \hat{b}_{e,\ell}^\dagger, \\ \hat{\rho}_{e,\ell < 0} &= \sqrt{\nu_e |\ell|} \hat{b}_{e,\ell}. \end{cases} \quad (\text{S41})$$

In the other case, i.e. when $\nu_e < 0$, we instead have

$$\begin{cases} \hat{\rho}_{e,\ell > 0} &= \sqrt{-\nu_e |\ell|} \hat{b}_{e,\ell}, \\ \hat{\rho}_{e,\ell < 0} &= \sqrt{-\nu_e |\ell|} \hat{b}_{e,\ell}^\dagger. \end{cases} \quad (\text{S42})$$

Using these identifications together with Eq. (S38), one can thus rewrite the $\ell = \pm 1$ Fourier components of $\hat{\rho}_{\text{eff}}(\theta)$ as

$$\begin{aligned} \hat{\rho}_1 &= \sum_{e,\nu_e > 0} \sqrt{\nu_e} \hat{b}_{e,1}^\dagger + \sum_{e,\nu_e < 0} \sqrt{-\nu_e} \hat{b}_{e,1}, \\ \hat{\rho}_{-1} &= \sum_{e,\nu_e > 0} \sqrt{\nu_e} \hat{b}_{e,1} + \sum_{e,\nu_e < 0} \sqrt{-\nu_e} \hat{b}_{e,1}^\dagger. \end{aligned} \quad (\text{S43})$$

Analogously to the single-edge case, only a single state (for every edge mode e) $|e\rangle = \hat{b}_{e,1}^\dagger |0\rangle$ contributes to the relevant matrix elements $v_\pm^{n,0}$ in Eq. (S29). Namely,

$$\begin{aligned} v_+^{e,0} &= f(R) \sqrt{\nu_e}, \\ v_-^{e,0} &= f(R) \sqrt{-\nu_e}. \end{aligned} \quad (\text{S44})$$

The contributions from the two chiralities S_\pm [see Eq. (S27)] can therefore be evaluated as,

$$\begin{aligned} S_+ &= |f(R)|^2 \sum_{e,\nu_e > 0} \nu_e, \\ S_- &= |f(R)|^2 \sum_{e,\nu_e < 0} -\nu_e. \end{aligned} \quad (\text{S45})$$

Here, we note that none of these individual contributions is robustly quantized in terms of the many-body Chern number. However, the difference $S_+ - S_-$ is quantized, since

$$\begin{aligned} \Delta S &= S_+ - S_- \\ &= |f(R)|^2 \left(\sum_{e,\nu_e > 0} \nu_e + \sum_{e,\nu_e < 0} \nu_e \right) \\ &= |f(R)|^2 \sum_e \nu_e = |f(R)|^2 \nu, \end{aligned} \quad (\text{S46})$$

which is precisely the result quoted in the main text.

In the case of conventional circular dichroism (uniform circular driving), one sets $f(R) = R$ and the result can be written as

$$\Delta S = \frac{A}{\pi} |C_{\text{MB}}|. \quad (\text{S47})$$

We conclude this section with a series of comments and remarks. Here, we explicitly assumed that: (i) the various edges are sufficiently close to each other, such that they are all located at $r \simeq R$; and (ii) we assumed that these edges are well separated one from the other. The first assumption (i) should not be harmful in the thermodynamic limit, provided the confinement is steep, since the particle density can be expected to suddenly drop from its bulk value $\rho_0 = \frac{\nu}{2\pi l_B^2}$ to zero. However it must be noticed that this is not always the case, especially in the case of smooth confining potentials, where “wedding-cakes” of different filling fractions can be expected [88]. On the other hand, we do not expect the second assumption (ii) to be crucial, provided that when the edges are brought together there exists a unitary mapping between the two sets of modes (i.e. those associated to the “far-away” edges and the ones of the “close-by” case).

The case of non-circular boundaries

We finally demonstrate that the total circular dichroic response in Eq. (S37) does not rely on the boundary being circular. Specifically, we will now consider QH droplets whose shape is determined by some externally imposed confinement potential, of arbitrary shape [56]. In this case, the boundary of the QH system will follow one of the equipotential lines of the confinement, provided the QH droplet is large enough ($N \gg 1$) and the equipotential does not have “too sharp” features (on the scale set by the magnetic length l_B). For the sake of simplicity, we hereby consider the case of a single chiral edge mode propagating along this non-trivial geometry.

We consider a convenient set of (action-angle [56]) coordinates (K, Θ) in terms of which we express the Cartesian coordinates

$$\begin{cases} x = F(K, \Theta) \\ y = G(K, \Theta). \end{cases} \quad (\text{S48})$$

Curves at constant K describe, at least locally at the position of the system’s boundary, equipotential lines for the confinement, i.e. they follow the system’s boundary. Notice that the angle variable Θ does not necessarily correspond to the polar angle [56].

The boundary will thus be parameterized by a curve described by a specific value of K , say $K = K_{\text{edge}}$. We decompose the parametric representation of the boundary in Fourier modes as

$$\begin{cases} x = F(K_{\text{edge}}, \Theta) = \sum_{\ell} e^{i\ell\Theta} f_{\ell}, \\ y = G(K_{\text{edge}}, \Theta) = \sum_{\ell} e^{i\ell\Theta} g_{\ell}. \end{cases} \quad (\text{S49})$$

Here, since $F(K_{\text{edge}}, \Theta)$ and $G(K_{\text{edge}}, \Theta)$ are real valued, $f_{-\ell} = f_{\ell}^*$ and $g_{-\ell} = g_{\ell}^*$.

We now compute the relevant transition matrix elements [see Eq. (S18)],

$$v_{\pm}^{n,0} = \int (x \pm iy) \langle n | \hat{\rho}(\mathbf{r}) | 0 \rangle d\mathbf{r}. \quad (\text{S50})$$

On the system’s boundary, one can approximate $x \pm iy$ using Eq. (S49) and obtain

$$v_{\pm}^{n,0} = \sum_{\ell} (f_{\ell} \pm ig_{\ell}) \int e^{i\ell\Theta} \langle n | \hat{\rho}_{\text{eff}}(\Theta) | 0 \rangle d\Theta, \quad (\text{S51})$$

where, in analogy with Eq. (S30), we identify the K integral of the two-dimensional particle density operator $\hat{\rho}(\mathbf{r})$,

$$\hat{\rho}_{\text{eff}}(\Theta) = \int \hat{\rho}(x(K, \Theta), y(K, \Theta)) dK, \quad (\text{S52})$$

as the effective one-dimensional density operator of the χ LL theory. Therefore, (analogously to Eq. (S33) and Eq. (S34)), the Fourier components $\hat{\rho}_{\ell} = \int e^{i\ell\Theta} \hat{\rho}_{\text{eff}}(\Theta) d\Theta$ can be identified with bosonic creation/annihilation operators, and the excited edge-states $|n\rangle$ as states in which χ LL quanta have been inserted by acting with bosonic creation operators on the vacuum state $|0\rangle$. With these identifications, we obtain

$$v_{\pm}^{n,0} = \sqrt{\nu n} (f_n \pm ig_n), \quad (\text{S53})$$

and thus

$$S_{\pm} = |C_{\text{MB}}| \sum_{n>0} n |f_n \pm ig_n|^2. \quad (\text{S54})$$

Here, we again identified $|C_{\text{MB}}| = \nu$. Importantly, in contrast with the circular-geometry case, S_{-} does not necessarily vanish in the presence of an arbitrary edge geometry.

After simple algebraic manipulations, the differential rate $\Delta S = S_{+} - S_{-}$ can finally be written as

$$\Delta S = |C_{\text{MB}}| \frac{1}{\pi} \left(-2\pi i \sum_{n>0} n (f_n g_n^* - f_n^* g_n) \right). \quad (\text{S55})$$

We notice that the area of the quantum Hall system coincides with the area enclosed by the parametric curve in Eq. (S49) and can be written as

$$A = \frac{1}{2} \oint (x dy - y dx) = -2\pi i \sum_{\ell>0} \ell (f_{\ell} g_{\ell}^* - f_{\ell}^* g_{\ell}), \quad (\text{S56})$$

which is the same expression appearing on the right hand side of Eq. (S55). We therefore recover the general result,

$$S_{+} - S_{-} = \frac{A}{\pi} |C_{\text{MB}}|. \quad (\text{S57})$$

This demonstrates that the edge-dichroic response is entirely low-energy in nature and it is quantized, even for

general boundary shapes. In this case, both S_{\pm} contribute to the response, and their specific values are dictated by the shape of the system's boundary. However, their difference depends on the geometry only through the system's area, A . In fact, and as we further discuss below, their ratio S_-/S_+ measures the anisotropy of the boundary.

Examples and numerical results

Here, we consider the anisotropic droplets described in Ref. [56] as a concrete example. In particular, we consider a confinement potential given by

$$V_{k,\lambda}(r, \theta) = \frac{u_0}{2} r^2 (\cosh(2\lambda) + \cos(k\theta) \sinh(2\lambda)), \quad (\text{S58})$$

with polar coordinates r, θ , and k is an integer, while u_0 and λ set the scale and deformation's magnitude of the confinement, respectively. We point out that the specific analytical form of the confinement, deep in the incompressible bulk, is irrelevant for the results; all that matters, indeed, is the shape of the edge.

In terms of the angle coordinate Θ , the polar angle θ reads

$$\theta(\Theta) = \frac{1}{k} \arg \left(\frac{\sinh(\lambda) - e^{ik\Theta} \cosh(\lambda)}{-\cosh(\lambda) + e^{ik\Theta} \sinh(\lambda)} \right) + 2\pi \frac{n}{k}, \quad (\text{S59})$$

where $n = 0, 1, \dots, k-1$. The shape of the boundary in Eq. (S49) can then be expressed as

$$\begin{cases} \frac{x/l_B}{\sqrt{2K_{\text{edge}}}} = \sqrt{\cosh(2\lambda) - \cos(k\Theta) \sinh(2\lambda)} \cos(\theta(\Theta)), \\ \frac{y/l_B}{\sqrt{2K_{\text{edge}}}} = \sqrt{\cosh(2\lambda) - \cos(k\Theta) \sinh(2\lambda)} \sin(\theta(\Theta)), \end{cases} \quad (\text{S60})$$

which allows for the numerical computation of S_{\pm} as given in Eq. (S54).

We notice that, in the present case, K_{edge} only appears as a scale factor for the boundary shape. As a consequence, the only dependence of f_l and g_l on K_{edge} is of the form $\sqrt{K_{\text{edge}}}$ and thus in the thermodynamic limit (when the low-energy edge description holds) the ratio S_-/S_+ depends only on the geometry of the boundary.

We now discuss the two cases $k = 2$ and $k = 3$.

The $k = 2$ case — In this case, the potential in Eq. (S58) has a simple quadratic form,

$$V_{2,\lambda}(r, \theta) = \frac{u_0}{2} (e^{2\lambda} x^2 + e^{-2\lambda} y^2). \quad (\text{S61})$$

This deformed potential is relevant for rapidly rotating atomic gases [89].

The boundary shape in Eq. (S60) simplifies to

$$\begin{cases} x/l_B = \sqrt{2K_{\text{edge}}} e^{-\lambda} \cos(\theta), \\ y/l_B = \sqrt{2K_{\text{edge}}} e^{+\lambda} \sin(\theta), \end{cases} \quad (\text{S62})$$

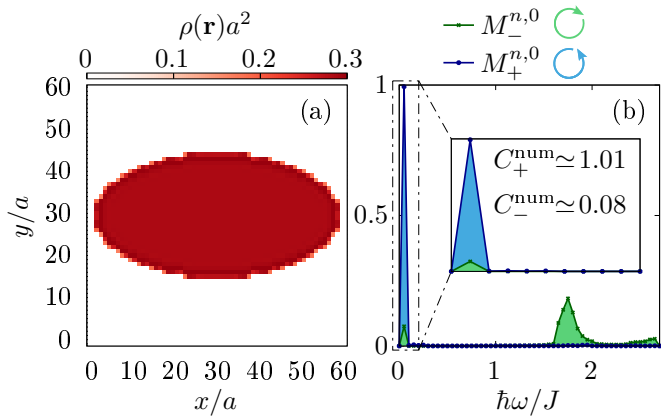


FIG. S1. (a) Ground state density for a non-interacting fermionic CI, confined by an elliptically-shaped box; the ratio between the two semiaxis of the trap, Δx and Δy , was fixed to $\Delta x/\Delta y = 1.97$. The flux per plaquette has been fixed to $\phi = 2/7$, and the Fermi energy approximately in the middle of the first gap, $\varepsilon_F = -1.5J$. (b) CD matrix elements $M_{\pm}^{n,0}$ [Eq. (5)], as a function of the excitation frequency $\omega_{n,0}$, with the inset zooming in on the low-energy features. The numerically extracted Chern number contributions, $C_{\text{MB}}^{\text{num}} = C_+^{\text{num}} - C_-^{\text{num}}$, are calculated by isolating the low-energy response ($\hbar\omega \leq 1J$).

which is an ellipse with an enclosed area $A = 2\pi K_{\text{edge}} l_B^2$. Furthermore, from Eq. (S54), we obtain

$$\begin{aligned} S_+ &= |C_{\text{MB}}| 2K_{\text{edge}} l_B^2 \cosh^2(\lambda), \\ S_- &= |C_{\text{MB}}| 2K_{\text{edge}} l_B^2 \sinh^2(\lambda), \end{aligned} \quad (\text{S63})$$

which, as expected on the more general grounds exposed above, satisfies $\Delta S = |C_{\text{MB}}| 2K_{\text{edge}} l_B^2 = |C_{\text{MB}}| A/\pi$. Furthermore, the ratio

$$\frac{S_-}{S_+} = \tanh^2(\lambda), \quad (\text{S64})$$

is indeed K_{edge} independent, and thus also independent of the number of particles; rather, it reflects the boundary ellipticity.

We show in Fig. S1 the results obtained in the case of a CI on the lattice [see Eq.(6)], without the elliptical harmonic trap Eq. (S61) but rather with an elliptical box potential. It can be seen that the results we presented do hold also in this case. In particular, (i) S_- does not vanish; (ii) the difference $S_+ - S_-$ is quantized in terms of the many-body Chern number, in agreement with Eq. (S57); (iii) the ratio $S_-/S_+ \approx 0.08$ is accurately described by Eq. (S64); λ can indeed be obtained from the ratio between the two semi-axes of the ellipse according to Eq. (S62). For the elliptical box confinement we considered, $\frac{\Delta x}{\Delta y} = e^{-2\lambda} \simeq 1.97$; Eq. (S64) then gives $S_-/S_+ \simeq 0.1$, which approximately agrees with the value we numerically extract. We attribute the difference to finite size effects on the lattice, but postpone more extensive and systematic investigation to future studies.

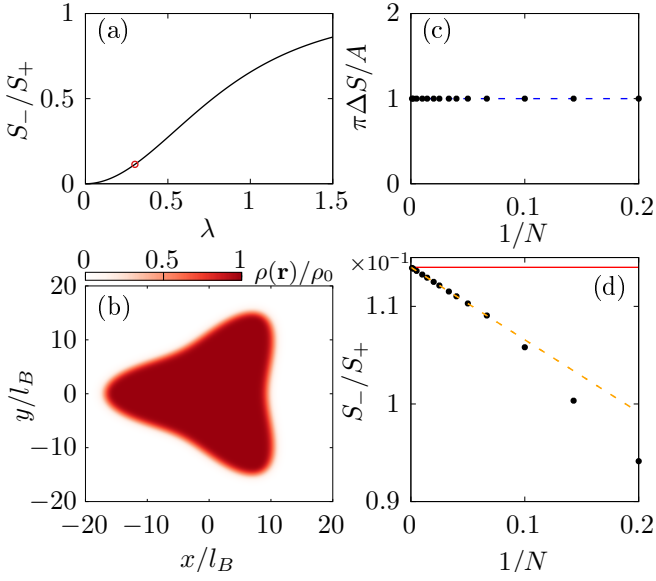


FIG. S2. (a) Numerically computed χ LL value of the ratio of S_-/S_+ as a function of the trap deformation factor λ , for $k = 3$ (see Eq. (S58)). The red circle identifies the value $\lambda = 0.3$ used in the other panels. (b) Ground state density $\rho(\mathbf{r})$ for an integer quantum Hall system of $N = 80$ fermions in the non-circularly symmetric potential in Eq. (S58). The density $\rho(\mathbf{r})$ has been normalized to the bulk one, $\rho_0 = \frac{1}{2\pi l_B^2}$. (c) The circular dichroic response ΔS as a function of the number N of particles in the two-dimensional trap. (d) The ratio S_-/S_+ as a function of the number of particles is compared with the value computed in panel (a). The red line $S_-/S_+ \simeq 0.114$ is approached $\propto 1/N$ as the size of the system is made larger; in the scaling limit (orange dashed line) we extract $S_-/S_+ \simeq 0.114$, in accordance with the theory.

The $k = 3$ case — In this case, to the best of our knowledge, it is not possible to rewrite Eq. (S49) in simple terms. However, as anticipated, we can use these relations to compute the ratio S_-/S_+ numerically (through the use of Eq. (S54)) and compare it with numerical results obtained by performing exact-diagonalization for a system of non-interacting fermions in the lowest-Landau level confined by Eq. (S58).

In Fig. S2(a), we show the numerically computed theoretical ratio S_-/S_+ as a function of λ . In Fig. S2(b), we show the ground state density $\rho(x, y)$ for $N = 80$ non-interacting fermions, for a fixed value of $\lambda = 0.3$. For the same value of λ , in Fig. S2(c,d) we show as a function of the number of particles N that ΔS is quantized in accordance with Eq. (S57) and that as the system is made larger the theoretical prediction for the ratio S_-/S_+ is approached.